A New 4D-RGB Mapping Technique for Field-Based High-Throughput Phenotyping

Ali Shafiekhani[1]
Ashafiekhani@mail.missouri.edu
Felix B. Fritschi[2]
FritschiF@missouri.edu
Guilherme N. DeSouza[1]
DeSouzaG@missouri.edu

[1] ViGIR Lab
Dept. of Electrical Engineering and Computer Science
[2] Division of Plant Sciences
University of Missouri
Columbia, MO, USA

Abstract

In this paper, we proposed the use of Infrared Thermography (IRT) along with multi-view, visible imaging technology to monitor plants 24/7 and to better understand their behavior in response to different biotic and/or abiotic stresses. The proposed method uses a high-throughput plant phenotyping platform previously developed by the authors: in special an observation tower that collects data throughout the growing season. Stereo RGB and Thermal images are used to create *4D-RGB models* of the canopy: i.e. their 3D appearance with temperature and texture information. We evaluate the accuracy of our thermal projection using quantitative and qualitative analysis and the results show high spatial consistency between appearance and temperature. The usefulness of our proposed 4D-RGB point cloud is demonstrated for two test cases: 1) over various days during the growing season; and 2) over various hours throughout the daytime.

1 Introduction

Temperature is an important and informative measure and it is often obtained by Infrared Thermography (IRT). Infrared thermography gives an image of an object where each pixel represents the temperature of a corresponding point on the surface of the object. The temperature is obtained by measuring the amount of infrared light, invisible to the human eye, emitted by the object due to its thermal conditions [20]. The most important characteristics of IRT are that it is a non-destructive and non-contact measurement, which makes the measurements safe and appropriate for a large range of applications in industries like aerospace, automotive, electronics, metallurgy and disciplines such as medicine, agriculture and military [17].

In the past few years, this technology has advanced immensely with less expensive, smaller, and lighter thermal cameras, which yet provide higher resolution and more accuracy. These advances made thermal cameras even more appropriate and accessible for a growing number of applications., such as: diagnostics of buildings regarding energy consumption [12]; inspection of small electronics to large pipes [2, 12, 27]; firefighting by providing clear view through the smoke [19]; etc. In fact, the new cameras' small sizes and weight allowed them to be mounted on small unmanned aerial vehicles (UAVs), which opened the door

to a variety of applications from law enforcement and military surveillance [13, 16, 31] to agriculture [11] and energy efficiency [1, 22].

As expected, IRT has also demonstrated great impact in agriculture and food industry. That is, from plant phenotyping to food preparation, we find IRTs in: water stress evaluation; irrigation scheduling; disease and pathogen control; yield prediction; fruits maturity identification; detection of foreign bodies in food material; and temperature distribution during cooking, to site a few [26, 29]. In plant phenotyping for example, a measure of interest is the rate of evaporation or transpiration from a leaf, which influences the leaf surface temperature [21]. Thermal imaging along with other imaging techniques have been widely used to study how plants are responding to different biotic and/or abiotic stresses [14]. The canopy temperature measured by thermal cameras can identify differences in stomatal conductance of different families of plants in response to their water status and transpiration rate [10, 18].

Although IRT provides less accuracy compared to contact-based methods [2], the aforementioned characteristics still make it more suitable for agriculture and plant phenotyping [23]. However, thermal images suffer from low contrast specially when the object of interest has a similar temperature as the background. Specifically, georeferencing a thermal image is sometimes difficult and often done by visual inspection of the IR image of the object in search for peculiar thermal regions. This limitation is caused mainly by the 2D projection of 3D objects, where information on the geometry and location of the objects and their surrounding areas are lost or *blended* due to their similar temperatures.

Fusion of thermal images with other imaging technologies can provide richer information depending on the application. For instance, Chaerle et al. studied plant populations using combined thermal and chlorophyll fluorescence imaging [5]. They showed that while thermal imaging is capable of monitoring stomatal responses, fluorescence imaging can give information about photosynthesis and, when combined, they can be used to derive leaf water use efficiency.

The 3D representation of objects captured by different imaging technology is a growing area and has shown a great impact on different disciplines. Among different 3D sensors, depth sensors (e.g. Microsoft Kinect) are more popular due to their low price and relative high accuracy in 3D mapping. Fusion of depth information with thermal image was studied in [30], where the authors introduced a handheld device built using a Kinect 360 and a Thermoteknix Miricle 307K thermal camera. The resulting 3D dense point cloud contained both visible RGB and surface-temperature information of the objects. However, most RGBD cameras (i.e. RGB+depth) are designed for close-up (1-5m) imaging and limited to indoor-like conditions, where no sunlight can interfere with the sensors. So, to overcome these limitations, the combination of 3D LiDAR and thermal camera for outdoor conditions was studied in [9] where a mobile robot was equipped with a Riegl VZ-400 laser 3D scanner and an optris PI160 thermal camera. Although 3D laser scanners are able to collect accurate 3D point cloud in outdoor conditions, the cost of a 3D laser scanner is often too high for most research programs.

In this paper, we propose the use of a trinocular camera rig consisting of a stereo RGB pair plus a thermal camera to create multi-dimensional models of the plants in the field. That is, our system allows both appearance and temperature information to be stored and analyzed for plant phenotyping purposes. We refer to it as a 4D-RGB model, since structural (3D), thermal (+1D) and textural (RGB) information are accurately registered and stored. To the best of our knowledge, the proposed system is the first to use stereo cameras in combination with a thermal camera to provide such rich information for phenotyping. In [3] for example, the authors use multi-dimensional data (RGB, thermal, etc...) to calculate some indices of

interest for phenotyping. However, even though their system georeferenced all the different data, the final result was a combination of independent TIF files and the system did not fuse all the acquired data into a single model for visualization and analysis as we propose here. Therefore, the main contributions of this paper are:

- Outdoor 4D-RGB mapping using a stereo RGB pair and a thermal camera
- The application of thermal 3D mapping in plant phenotyping
- 4D-RGB visualization of a plant canopy throughout the day and the season (over time)

The rest of this paper is organized as follows: in section 2 the overall hardware and software developed for 4D-RGB mapping is described. In this section, the calibration procedures, 3D reconstruction pipeline and fusion of thermal-visible information with 3D point cloud are discussed in detail. In section 3, after providing quantitative and qualitative evaluation of our proposed system, results for 4D-RGB modeling of the canopy are provided for two test cases: over various days during the growing season and over various hours throughout the daytime. Finally, in section 4 we conclude and discuss future applications of our proposed system for plant phenotyping.

2 Material and Methods

2.1 Platform

In this paper we used a high-throughput field-based plant phenotyping platform, Vinoculer – for ViGIR-Lab Phenotyping Trinocular Observer [24, 25]. Vinoculer consists of a mobile observation tower equipped with a stereo RGB setup (two 12 M pixel Grasshopper3 cameras) and a thermal camera (Flir A625) centered between RGB cameras. Sensors were mounted on a turn table to rotate 360° and oversee the entire field. The turn table can position the sensor platform with 0.1° accuracy. A temperature sensor was also mounted on the platform to measure air temperature. Figure 1 shows the mobile observation tower deployed in the middle of a corn field. The entire system was powered through $12V$ lead-acid batteries, which were charged through solar panels, but could last two days without sunlight. The entire system was weatherized to tolerate typical summer conditions i.e., over $100°F$ $(37.8°C)$ temperatures, rain, and strong winds (maximum winds of $50\,mph$ or $22.3\,m/s$ were recorded in the period of deployment).

2.2 Calibration

Camera calibration is an essential step when dealing with images. There are different types of calibrations (thermal calibration, color calibration, geometric camera calibration, stereo camera calibration, head-eye calibration) and some were used in this paper. For instance, thermal cameras are very sensitive and have to be calibrated regularly in order to produce accurate measurements. This calibration usually is conducted using black bodies, which avoid spurious radiation reflectivity, often provided by the manufacturer as well as many laboratories around the world. Below, some of the calibration procedures used in this paper are described briefly:

Figure 1: Mobile Observation Tower with two RGB cameras and a thermal camera in between

Geometric Camera Calibration

Geometric calibration is an important step in which one finds a mathematical model relating the image pixel coordinates to their corresponding points in 3D space. This is commonly done using a chessboard with black and white squares that makes corner detection easy. For RGB cameras, this is relatively straight forward since a normal chessboard with black and white color can be used to calibrate the camera; however, a thermal camera is not able to detect black and white squares since the camera returns the temperature of squares. In this work, we developed a calibration pattern using a multi-material surface: i.e., thin black painted Aluminum squares on top of white paper. This combination of highly heat-absorbent and highly heat-reflective materials created enough contrast for detecting corners and producing an accurate calibration – even on cloudy days. The developed pattern measured $1.5m(H) \times 1.5m(W)$, with 81 black aluminum squares ($8 \times 8\,cm^2$ each). The black aluminum and white paper squares were applied to a foam board and mounted on a sturdy, but light wooden frame to provide support for the foam-board and two handles on the back – allowing for easy positioning of the pattern during calibration. A popular camera calibration algorithm [32] and its widely available implementation [28] were used to calibrate all three cameras with images captured at 10 different positions and orientations of the calibration pattern.

Stereo Camera Calibration

In addition to individual camera calibration which results in intrinsic and distortion camera parameters, stereo camera calibration was done for left-thermal cameras and left-right cameras. To determine the position and orientation of the cameras with respect to each other, the first calibration was executed to obtain the correct association between the measurement of the temperature and the reconstructed 3D model of plants. Figure 2 shows three of those images, one for each of the cameras being calibrated.

Head-eye Calibration

In mobile robotic applications, the problem of finding the camera coordinate frame with respect to the mobile robot frame is usually referred to as *head-eye* calibration and it can be

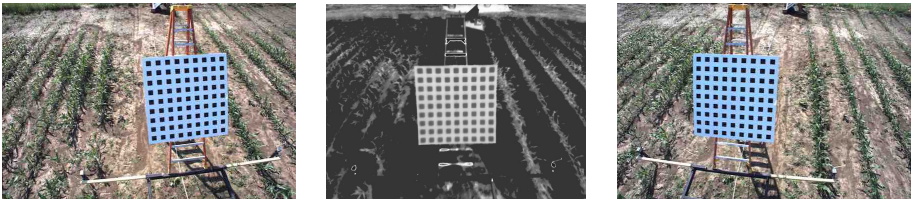

(a) Left Image (b) Thermal Image (c) Right Image

Figure 2: Three typical images of the aluminum + paper pattern used for calibration of RGB and IR cameras. (a) Left RGB; (b) IR Image; (c) Right RGB

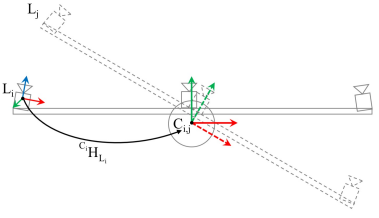

Figure 3: Coordinate frame of left camera with respect to turn-table (head-eye calibration)

formulated as a $AX = XB$ system of equations, where X is the unknown position/orientation (or pose) of the camera frame, and A and B are known reference frames. In this paper, we used an iterative method developed by DeSouza et al. [8] to find the pose of the left camera with respect to the world coordinate frame attached to the turn table. Figure 3 illustrates the transformation incurred by the left camera while capturing one of the ten images obtained of the pattern at a fixed pose – i.e. ten images at different angles of the turn table such as the ones shown in Figure 2. For two reasons the head-eye calibration is an important step in our 4D-RGB reconstruction pipeline. First, the obtained point cloud can be referenced to a single world coordinate frame – i.e. fixed with respect to the field. This makes the phenotype features (e.g. height) and their localization in a specific plot possible. Second, all camera poses can be initially estimated with respect to the turn-table's encoder, which makes the 3D reconstruction process faster (see our Constrained Bundle Adjustment below).

2.3 3D Reconstruction Pipeline

Our 3D reconstruction pipeline consists of five steps: 1) sparse feature extraction and matching between stereo cameras for two consecutive frames using three-view matching; 2) sparse 3D point calculation using triangulation between left and right cameras; 3) camera poses estimation as an initial guess; 4) camera poses refinement by running a Constrained Bundle Adjustment (CBA); and 5) dense 3D reconstruction. These steps are detailed below.

Feature Extraction and Matching

In order to create 3D point clouds and determine relative camera poses, we must find a series of corresponding 2D points between a pair of corresponding left (L_i) and right (R_i) images in addition to a consecutive frame pose of the left camera L_{i+1} – here, i represents the image sequence obtained at the $i-th$ angle of the turning table. In this paper, we used SIFT feature

descriptor [15] to perform three-view matching between L_i, R_i, and L_{i+1}. Undistorted and resized images were used to speed up feature extraction and matching. These 2D points were re-scaled to the original image size for the next steps.

Triangulation

Using the calibration parameters obtained for the stereo camera rig and triangulation technique, 3D coordinates are calculated for all matching 2D feature points. These 3D coordinates are for points visible in both the left and right camera images and are calculated with respect to the left camera coordinate frame i.

Camera Pose Estimation

Relative camera poses between consecutive left frames were found by minimizing the sum of re-projection errors of 3D points onto the next left frame. Given intrinsic parameters of the left camera, the re-projection onto the next left frame can be calculated by:

$$\begin{pmatrix} u \\ v \\ 1 \end{pmatrix} = K_{left} \begin{bmatrix} R(\overrightarrow{r}) & \overrightarrow{t} \end{bmatrix} \begin{pmatrix} X \\ Y \\ Z \\ 1 \end{pmatrix} \tag{1}$$

where $R(\overrightarrow{r})$ and $\overrightarrow{t}$ are rotation and translation of transformation from the left camera coordinate frame at instant (angle of the turntable) i and $i+1$; K_{left} is the 3×3 intrinsic matrix for left camera and $[X,Y,Z]^T$ is the 3D coordinate of a point in the $i-th$ left camera coordinate frame. Using the *Perspective from n Points* algorithm (PnP) [9], the rotation, $R(\overrightarrow{r})$, and the translation, $\overrightarrow{t}$, were found while minimizing the re-projection error. Given relative rotations and translations, transformation from the $i-th$ left frame to the world coordinate frame attached to the base can be expressed as a chain of transformations:

$${}^{w}H_{L_i} = {}^{w}H_{L_1} \times {}^{L_1}H_{L_2} \times \cdots \times {}^{L_{i-1}}H_{L_i} \tag{2}$$

where ${}^{w}H_{L_1}$ was obtained from the head-eye calibration. This step can be optionally replaced using the turntable's yaw angle recorded for each frame:

$${}^{w}H_{L_i} = {}^{w}H_{C_i} \times {}^{C_i}H_{L_i} \tag{3}$$

where ${}^{C_i}H_{L_i}$ was also found by head-eye calibration. ${}^{w}H_{C_i}$ is the transformation incurred by a simple rotation about the z axis (yaw) and is given by:

$${}^{w}H_{C_i} = \begin{bmatrix} \cos(\theta_i) & -sin(\theta_i) & 0 & 0 \\ sin(\theta_i) & \cos(\theta_i) & 0 & 0 \\ 0 & 0 & 1 & 0 \\ 0 & 0 & 0 & 1 \end{bmatrix} \tag{4}$$

We obtained similar results for the 3D reconstruction using either eq. (2) or (3) above, with one additional caveat. That is, although the use of PnP (eq. (2)) takes longer than the simpler calculation of the camera poses from the turntable's yaw angle (eq. (3)), its additional step of eliminating 3D point outliers compensates for the extra time by speeding up the refinement of camera poses in the next step. So, the optimum result was obtained

by taking advantage of the simpler and faster camera poses calculation from the turntable's angle and adding a step to filter any 3D point outliers using RANSAC.

Bundle Adjustment

In order to refine the camera poses, a Constrained Bundle Adjustment (CBA) was developed using a specific constraint: the cameras rotate about a fixed z axis (yaw). With this constraint, instead of having to determine $6 \times N$ unknowns, where N is the number of left frames for which 6 rotational and translational parameters are unknown, only $6+N$ unknowns were parametrized for refinement. These $6+N$ unknowns are in the expressions of ${}^{C_i}H_{L_i}$ and ${}^{w}H_{C_i}$ above – that is, they are the 6 parameters for refinement of the head-eye calibration and the remaining N parameters for refinement of θ_i. Once the left camera poses were obtained, the right camera poses could be found using the stereo camera calibration parameters (${}^{L}H_{R}$):

$$ {}^{w}H_{R_i} = {}^{w}H_{L_i} \times {}^{L}H_{R} \tag{5} $$

Compared to global bundle adjustment with $6 \times N$ unknowns, this simplification not only led to faster convergence (only 10 iterations as opposed to 50) but also reduced the convergence residual error from ~ 4.1 to ~ 0.07, and as a result it improved the dense reconstructed point cloud visualized in section 3.

Dense 3D Reconstruction

In this paper, we used the multi-view dense reconstruction algorithm developed by Furukawa and Ponce [8] to create a dense 3D point cloud. We used output of PMVS2 (*.patch full reconstruction information) to create the 4D-RGB point cloud described next.

2.4 4D-RGB Point Cloud

In order to find the temperature of a 3D point, 3D-2D correspondences between world coordinate frame and thermal frame are required. This relation was found by stereo camera calibration between left and thermal cameras (${}^{T}H_{L}$).

$$ \begin{pmatrix} u \\ v \\ 1 \end{pmatrix} = K_{thermal} \begin{bmatrix} R & t \end{bmatrix} \begin{pmatrix} X \\ Y \\ Z \\ 1 \end{pmatrix} \tag{6} $$

where R and t are rotation and translation of transformation from world coordinate frame to $i-th$ thermal frame ${}^{T_i}H_{w}$:

$$ {}^{T_i}H_{w} = {}^{T_i}H_{L_i} \times {}^{L_i}H_{w} \tag{7} $$

Given the frame ID, k, from which the 3D point was reconstructed, one can find the temperature by re-projecting it back onto the thermal frame k. In this paper, the information provided by PMVS2 software was extracted and used to find the temperature of a 3D point in all visible thermal frames. To eliminate outliers, the median of these temperature values was assigned as the corresponding temperature ($\begin{bmatrix} X & Y & Z & R & G & B & T \end{bmatrix}$).

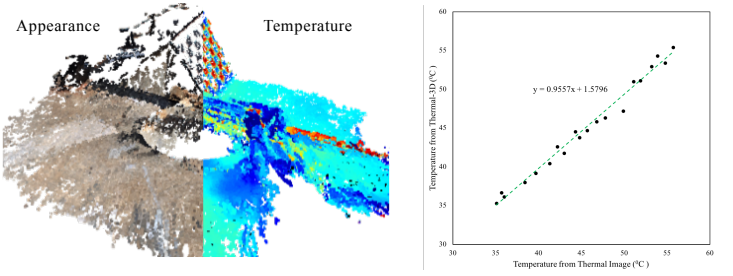

(a) (b)

Figure 4: (a) RGB(left) – Thermal (right) 3D model used for quantitative evaluation of thermal 3D projection. (b) Temperature of distinct points (in RGB and Thermal images) visible in point cloud and thermal image are compared.

3 Results:

In this section, results for our pipeline for 4D-RGB reconstruction of plants at different DAPs (days after planting) and different hours during a day are illustrated. These results were obtained based on data collected during the summer of 2016, from a field with different genotypes of corn (*Zea mays L.*) and sorghum (*Sorghum bicolor L.*). The field was planted in two different rows spacing, 30", and 45" for biological and technical purposes.

3.1 Validation of Thermal to 3D projection

In order to validate 4D-RGB reconstruction, quantitative and qualitative analysis were conducted. In the quantitative evaluation shown in Figure 4(b), the temperature of distinct points (visible both in RGB and Thermal images with two adjacent materials) are measured from point cloud and thermal image. All points were manually selected and the temperature from point cloud and thermal images are compared to show spatial consistency in projecting temperature information into the point cloud. This evaluation is done to ensure that the projection of thermal information into 3D point cloud has no offset or drift. Again, this can be more clearly tested at the edge between hot and cool materials as in the black and white squares in the calibration pattern, also depicted in Figure 4(a).

In terms of qualitative results, Figure 5(a) shows an analysis of the thermal projections where the RGB and temperature of plants in the field are both represented. As it can be seen through the rows of plants in the RGB (top) and Thermal (bottom) parts of the figure, the projection of the thermal signature on the point cloud is aligned with the true location of their 3D points. That is, rows of plants (easily visible in both RGB and Thermal) are perfectly aligned with each other without any offset.

3.2 4D-RGB Point Cloud of the Canopy

One of the main advantages of our developed platform (Vinoculer) is its ability of monitoring plants 24/7 and throughout the growing season. Also, fusion of thermal, RGB, and 3D point cloud opens the door to visualization, inspection and analysis through the extraction of important phenotypes that can correlate plant growth rate with the genotype and environmental conditions like temperature. Having the geometric information along with the

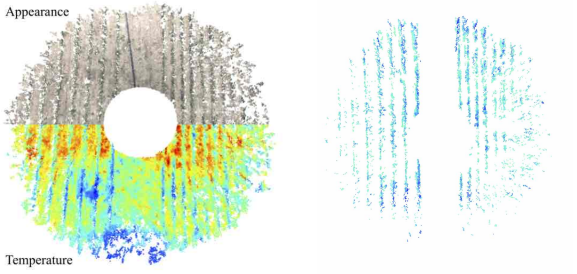

(a) (b)

Figure 5: (a) RGB (top) Thermal (bottom) 3D reconstructed point cloud of the entire field at 19 DAP (days after planting), (b) Canopy temperature by ground subtraction

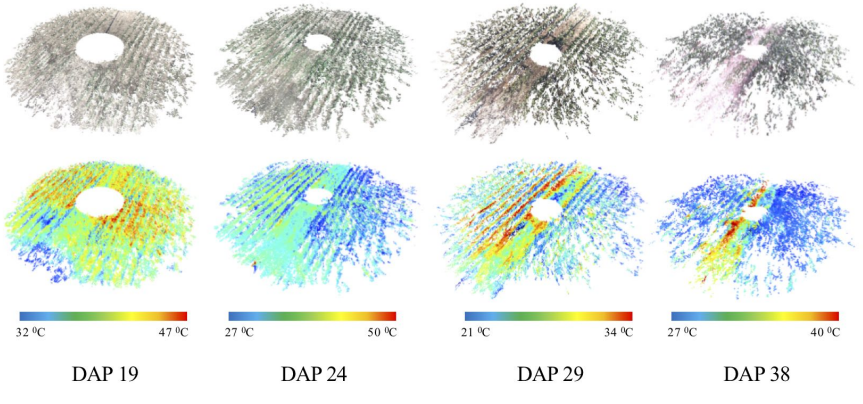

Figure 6: Snapshot of 4D-RGB models of the field throughout the season at four DAPs

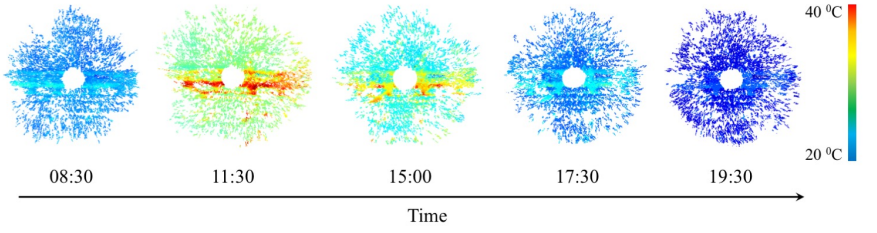

Figure 7: Snapshot of Thermal 3D models of the field at different times at 38 DAP

temperature can also help to maintain appropriate conditions for plants, for instance by irrigation of stressed areas of the field. Finally, visualization and analysis of 4D-RGB point cloud throughout the season allows us to better understand the long-term behavior of different genotypes.

In that sense, Figure 6 shows 3D models of the field with appearance and temperature information at four different DAPs (days after planting) 19, 24, 29, and 38. Similarly, Figure 7 shows the variation of temperature in the field throughout the day. For early developmental stages, when the canopy is not closed yet, both canopy and soil temperatures, two important measurements for plant biologists, can be extracted from thermal 3D. Having this information throughout the daytime when the field is under stress gives insight about the field conditions.

In order to illustrate some of analysis that can be performed with this 4D-RGB model, in Figure 5(b) we removed the ground plane of the field at 19 DAP, leaving only the canopy temperatures. This is important step of segmenting canopy from soil is made trivial by the 4D-RGB model by filtering the point cloud based on their Z coordinates. This is just one simple example of the potential information that can be obtained from the 4D-RGB model and used to study the behavior of different genotypes with respect to soil and air temperature, the effect of row spacing on different corn and sorghum hybrids, etc.

4 Conclusions and Future work

In agriculture and food industries, the use of technology is rapidly growing to improve food production both in quantity and quality. Imaging technology can greatly influence the industry by enabling researchers to measure important aspects. Fusion of plant data into 3D point cloud of the canopy enables and eases plant phenotyping where correspondence between plants and collected data is of great importance to researchers. Combination of RGB, Thermal and 3D point cloud over the growing season makes the interpretation of plant status in the context of environmental conditions easier (e.g. correlation between growth rate with average soil or plant temperature over the growing season). Our proposed 4D-RGB model of the field is capable of providing rich information such that many plant phenotypes can be extracted and correlated with each other and with plant performance. Plant characteristics for different genotypes, correlation between soil and leaf temperature, and effect of average temperature (heat stress) on growth rate are some of the topics the authors consider for future work using the developed pipeline for 4D-RGB reconstruction.

References

[1] Mohammadreza Aghaei, Edward Uzoma Madukanya, Aline Kirsten Vidal de Oliveira, and Ricardo Rüther. Fault inspection by aerial infrared thermography in a pv plant after a meteorological tsunami. In *VII Congresso Brasileiro de Energia Solar-CBENS 2018*, 2018.

[2] Aaron JE Bach, Ian B Stewart, Alice E Disher, and Joseph T Costello. A comparison between conductive and infrared devices for measuring mean skin temperature at rest, during exercise in the heat, and recovery. *PloS one*, 10(2):e0117907, 2015.

[3] Juliane Bendig, Kang Yu, Helge Aasen, Andreas Bolten, Simon Bennertz, Janis Broscheit, Martin L Gnyp, and Georg Bareth. Combining uav-based plant height from crop surface models, visible, and near infrared vegetation indices for biomass monitoring in barley. *International Journal of Applied Earth Observation and Geoinformation*, 39:79–87, 2015.

[4] Dorit Borrmann, Jan Elseberg, and Andreas Nüchter. Thermal 3d mapping of building façades. In *Intelligent autonomous systems 12*, pages 173–182. Springer, 2013.

[5] Laury Chaerle, Ilkka Leinonen, Hamlyn G Jones, and Dominique Van Der Straeten. Monitoring and screening plant populations with combined thermal and chlorophyll fluorescence imaging. *Journal of experimental botany*, 58(4):773–784, 2006.

[6] Guilherme Nelson DeSouza, Andrew H Jones, and Avinash C Kak. An world-independent approach for the calibration of mobile robotics active stereo heads. In *Robotics and Automation, 2002. Proceedings. ICRA'02. IEEE International Conference on*, volume 4, pages 3336–3341. IEEE, 2002.

[7] Hideki Endo and Takuya Kusaka. Efficient inspection for gas pipes by infrared thermography. *Kobelco Technology Review*, 33:50–55, 2015.

[8] Yasutaka Furukawa and Jean Ponce. Accurate, dense, and robust multiview stereopsis. *IEEE transactions on pattern analysis and machine intelligence*, 32(8):1362–1376, 2010.

[9] Xiao-Shan Gao, Xiao-Rong Hou, Jianliang Tang, and Hang-Fei Cheng. Complete solution classification for the perspective-three-point problem. *IEEE transactions on pattern analysis and machine intelligence*, 25(8):930–943, 2003.

[10] Hamlyn G Jones, Rachid Serraj, Brian R Loveys, Lizhong Xiong, Ashley Wheaton, and Adam H Price. Thermal infrared imaging of crop canopies for the remote diagnosis and quantification of plant responses to water stress in the field. *Functional Plant Biology*, 36(11):978–989, 2009.

[11] Sami Khanal, John Fulton, and Scott Shearer. An overview of current and potential applications of thermal remote sensing in precision agriculture. *Computers and Electronics in Agriculture*, 139:22–32, 2017.

[12] Angeliki Kylili, Paris A Fokaides, Petros Christou, and Soteris A Kalogirou. Infrared thermography (irt) applications for building diagnostics: A review. *Applied Energy*, 134:531–549, 2014.

[13] Frederik S Leira, Kenan Trnka, Thor I Fossen, and Tor Arne Johansen. A ligth-weight thermal camera payload with georeferencing capabilities for small fixed-wing uavs. In *Unmanned Aircraft Systems (ICUAS), 2015 International Conference on*, pages 485–494. IEEE, 2015.

[14] Lei Li, Qin Zhang, and Danfeng Huang. A review of imaging techniques for plant phenotyping. *Sensors*, 14(11):20078–20111, 2014.

[15] David G Lowe. Object recognition from local scale-invariant features. In *Computer vision, 1999. The proceedings of the seventh IEEE international conference on*, volume 2, pages 1150–1157. Ieee, 1999.

[16] Yalong Ma, Xinkai Wu, Guizhen Yu, Yongzheng Xu, and Yunpeng Wang. Pedestrian detection and tracking from low-resolution unmanned aerial vehicle thermal imagery. *Sensors*, 16(4):446, 2016.

[17] Carosena Meola. *Infrared thermography recent advances and future trends*. Bentham Science Publishers, 2012.

[18] Rana Munns, Richard A James, Xavier RR Sirault, Robert T Furbank, and Hamlyn G Jones. New phenotyping methods for screening wheat and barley for beneficial responses to water deficit. *Journal of experimental botany*, 61(13):3499–3507, 2010.

[19] Joseph J O Brien, E Louise Loudermilk, Benjamin Hornsby, Andrew T Hudak, Benjamin C Bright, Matthew B Dickinson, J Kevin Hiers, Casey Teske, and Roger D Ottmar. High-resolution infrared thermography for capturing wildland fire behaviour: Rxcadre 2012. *International Journal of Wildland Fire*, 25(1):62–75, 2016.

[20] Silvia Martın Ocaña, Ignacio Cañas Guerrero, and Ignacio González Requena. Thermographic survey of two rural buildings in spain. *Energy and Buildings*, 36(6):515–523, 2004.

[21] Ankush Prashar and Hamlyn G Jones. Infra-red thermography as a high-throughput tool for field phenotyping. *Agronomy*, 4(3):397–417, 2014.

[22] Tarek Rakha, Amanda Liberty, Alice Gorodetsky, Burak Kakillioglu, and Senem Velipasalar. Heat mapping drones: An autonomous computer-vision-based procedure for building envelope inspection using unmanned aerial systems (uas). *Technology| Architecture+ Design*, 2(1):30–44, 2018.

[23] P Rischbeck, P Cardellach, B Mistele, and U Schmidhalter. Thermal phenotyping of stomatal sensitivity in spring barley. *Journal of Agronomy and Crop Science*, 203(6): 483–493, 2017.

[24] Ali Shafiekhani, Suhas Kadam, Felix B Fritschi, and Guilherme N DeSouza. Vinobot and vinoculer: Two robotic platforms for high-throughput field phenotyping. *Sensors*, 17(1):214, 2017.

[25] Ali Shafiekhani, Felix B Fritschi, and Guilherme N DeSouza. Vinobot and vinoculer: from real to simulated platforms. In *Autonomous Air and Ground Sensing Systems for Agricultural Optimization and Phenotyping III*, volume 10664, page 106640A. International Society for Optics and Photonics, 2018.

[26] Soraya Shafiekhani, Shantae A Wilson, and Griffiths G Atungulu. Impacts of storage temperature and rice moisture content on color characteristics of rice from fields with different disease management practices. *Journal of Stored Products Research*, 78:89–97, 2018.

[27] Anna Vladova Stoynova and Borislav Borisov Bonev. Infrared survey in electrical preventive maintenance. In *Scientific Conference Electronics (ET), 2017 XXVI International*, pages 1–4. IEEE, 2017.

[28] Klaus Strobl, Wolfgang Sepp, Stefan Fuchs, Cristian Paredes, and Klaus Arbter. Camera calibration toolbox for matlab. *Pasadena, CA*, 2006.

[29] R Vadivambal and Digvir S Jayas. Applications of thermal imaging in agriculture and food industry: a review. *Food and Bioprocess Technology*, 4(2):186–199, 2011.

[30] Stephen Vidas, Peyman Moghadam, and Michael Bosse. 3d thermal mapping of building interiors using an rgb-d and thermal camera. In *Robotics and Automation (ICRA), 2013 IEEE International Conference on*, pages 2311–2318. IEEE, 2013.

[31] Yonghao Xiao, Hong Zheng, and Weiyu Yu. Automatic crowd detection based on unmanned aerial vehicle thermal imagery. In *International Conference on Mechatronics and Intelligent Robotics*, pages 510–516. Springer, 2017.

[32] Zhengyou Zhang. A flexible new technique for camera calibration. *IEEE Transactions on pattern analysis and machine intelligence*, 22(11):1330–1334, 2000.